PAPER • **OPEN ACCESS**

Validation of a multi-scale simulation strategy based on the Pointwise Strain Superposition Method

To cite this article: M Moda *et al* 2021 *IOP Conf. Ser.: Mater. Sci. Eng.* **1038** 012022

View the article online for updates and enhancements.

This content was downloaded from IP address 131.114.248.45 on 04/03/2021 at 15:43

Validation of a multi-scale simulation strategy based on the Pointwise Strain Superposition Method

M Moda[1,*], B D Monelli[1], M Benassi[2] and M Palladino[2]

[1] Department of Civil and Industrial Engineering, University of Pisa, Largo Lucio Lazzarino 2, 56122 Pisa PI, Italy

[2] Material & Process Engineering, Baker Hughes, Via Felice Matteucci 2, 50127 Florence FI, Italy

[*] Corresponding author: mattia.moda@ing.unipi.it

Abstract. This paper details the experimental validation of a multi-scale simulation strategy that we developed for predicting the stresses and distortions induced by Powder Bed Fusion processes. The strategy comprises a meso-scale model, a macro-scale model, and a scaling method named Pointwise Strain Superposition. The first model evaluates the temperature, stress, and strain fields produced by a single scan line. The scaling method transfers the meso-scale results to the macro-scale model, which is then able to simulate the entire manufacturing process with a reasonable computational cost. The simulation strategy was validated by comparing its results with the stresses and distortions measured on several specimens made of selective laser melted Inconel 718. Stresses were measured through the blind hole drilling method on a cylindrical specimen printed with two different scanning strategies, while distortions were measured on a hollow cylinder and on a cantilever-shaped specimen after removing its supports. In both cases the simulation showed first- or higher-order accuracy despite the significant uncertainties regarding the input parameters and material properties. This robustness, coupled with its computational efficiency, leads us to believe that our simulation strategy could enhance the process optimization and provide a better understanding of the underlying physical phenomena along with their effects on the manufactured parts.

1. Introduction

Designing and developing additively manufactured parts entails expensive and time-consuming trial and error procedures. This is partially due to process-induced stresses and distortions affecting the integrity and functionality of 3D printed components. Process simulation may thus be an efficient and effective approach to identify suitable or, preferably, optimal parameters and printing configurations based on the desired geometry and the adopted material.

This research focuses on validating a multi-scale simulation strategy that we developed to predict the residual stresses and distortions induced by Powder Bed Fusion (PBF) processes. Section 2 introduces the simulation method, while Section 3 discusses the validation procedure. Besides reporting the numerical and experimental results, we also provide their physical interpretation whenever appropriate. This approach broadens the scope of the paper beyond the specific geometries, material, and technology considered hereinafter.

2. Simulation strategy

From a theoretical perspective, PBF simulation differs from welding simulation mainly due to its vastly higher bead length-to-width ratios, which often exceed 10^8 unraveling the entire scanning path. This

Content from this work may be used under the terms of the Creative Commons Attribution 3.0 licence. Any further distribution of this work must maintain attribution to the author(s) and the title of the work, journal citation and DOI.
Published under licence by IOP Publishing Ltd

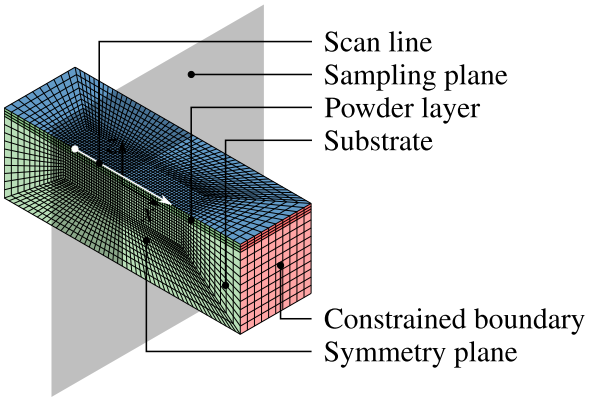

Figure 1. Meso-scale model.

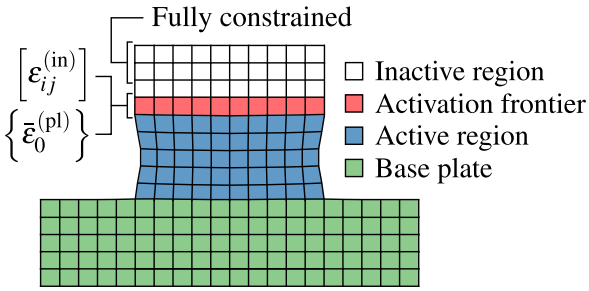

Figure 2. Macro-scale model.

prevents most welding simulation methods from being practically viable for PBF without reducing their computational cost. We thus developed a tailored multi-scale simulation strategy composed of a meso-scale thermo-structural model, a macro-scale purely structural model, and a scaling strategy named Pointwise Strain Superposition (PSS).

2.1. Meso-scale

The meso-scale model consists of a one-way coupled thermo-structural Finite Element (FE) simulation. It evaluates the thermal history along with the residual stress and strain fields produced by a single scan line under steady state conditions.

The modeled domain (Fig. 1) is symmetric about the plane $y = 0$ and large enough to allow a boundary condition of constant temperature with no displacement over those boundaries that do not face towards the build chamber. The top surface is stress-free and subjected to evaporative, radiative, and convective heat transfer.

The thermal load is applied through a moving Goldak heat source [1, 2] whose size and power are calibrated by minimizing the differences between the simulated and measured melted zones. Although not strictly necessary, this latter operation compensates for the uncertainties regarding the model hypotheses, energy absorptivity, and high-temperature thermophysical properties, which are rarely available with sufficient accuracy up to the boiling point.

Powder is considered a continuum with homogenized properties, and its densification implies a sudden increase in the thermal conductivity of the corresponding elements. In fact, melting and solidification are simulated by modifying the element stiffness and thermal conductivity. Furthermore, any plastic strain accumulated before and during the melting phase is reset upon solidification to simulate annealing and prevent unrealistic hardening effects.

Since the scanning process is performed under steady state conditions[1], and the domain approaches a state of rest during the cooling phase, the residual stress and strain fields are independent of x. This allows to reduce the output size as the results can be sampled on a plane perpendicular to x (e.g., $x = 0$ as represented in Fig. 1), provided that the selected sampling plane remains sufficiently distant from the scan line endpoints. The sampled meso-scale outputs can then be used to define the three interpolation functions $\varepsilon_{ij}^{(\mathrm{el})}(\mathbf{p})$, $\varepsilon_{ij}^{(\mathrm{pl})}(\mathbf{p})$, and $T_{\max}(\mathbf{p})$, which return the residual elastic and plastic strains, and the maximum temperature reached throughout the entire simulation given the position $\mathbf{p}$ on the sampling plane. By repeating the above procedure for every combination of process parameters employed for the selected material, we can build a database of interpolation functions whose records are associated with the corresponding material and parameter sets.

[1] The state variables are time-independent for an observer moving along with the heat source.

2.2. Pointwise Strain Superposition

The PSS method defines the incompatible strain $\varepsilon_{ij}^{(\mathrm{in})}$ and the initial equivalent plastic strain $\bar{\varepsilon}_0^{(\mathrm{pl})}$ of the macro-scale model (Section 2.3) based on the meso-scale results and the scanning strategy. In particular, $\varepsilon_{ij}^{(\mathrm{in})}$ is an inelastic strain component that reproduces the process-induced strain incompatibilities, while $\bar{\varepsilon}_0^{(\mathrm{pl})}$ represents the associated strain hardening.

The method relies on the following hypotheses:

(i) position independence: assuming equal material properties, process parameters, and pre-existing stress and strain fields, the effect of two identical scan lines is the same regardless of their position

(ii) steady state: by assuming uniform pre-existing stress and strain fields, each scan line is performed under steady state conditions, and the resulting residual stress and strain fields are independent of the coordinate parallel to the scanning direction

which can be relaxed by sacrificing either simplicity or efficiency, or both.

The values of $\varepsilon_{ij}^{(\mathrm{in})}$ and $\bar{\varepsilon}_0^{(\mathrm{pl})}$ are computed at one or multiple sample points inside each element of the macro-scale FE mesh through the Algorithm 1, where:

- $\wedge$ is the logical conjunction
- $\|\cdot\|$ is the Euclidean norm
- $\mathrm{tr}(\cdot)$ is the trace operator
- x, y, and z are the coordinates of the sample points
- n_l is the total number of scan lines needed to print the simulated part
- $A \in \mathbb{R}^{n_\mathrm{l}\times 3}$ is an array containing the coordinates of the start point for each scan line
- $B \in \mathbb{R}^{n_\mathrm{l}\times 3}$ is an array containing the coordinates of the end point for each scan line
- $F \in \mathbb{N}^{n_\mathrm{l}\times 1}$ is an array containing the reference to the interpolation functions for each scan line
- T_relax is the relaxation temperature (lower than or equal to the solidus)
- $\varepsilon_{ij,f}^{(\mathrm{el})}(\mathbf{p})$, $\varepsilon_{ij,f}^{(\mathrm{pl})}(\mathbf{p})$, and $T_{\mathrm{max},f}(\mathbf{p})$ are the f-th records in the database of interpolation functions
- R is a rotation matrix employed to express the interpolated strains in the global reference frame.

After applying the Algorithm 1 to every sample point, the strain values are averaged inside each element of the macro-scale mesh:

$$\left[\varepsilon_{ij}^{(\mathrm{in})}\right]_e = \frac{1}{n_e}\sum_{\mathbf{r}\in\Omega_e}\varepsilon_{ij}^{(\mathrm{in})}(\mathbf{r}) \tag{1}$$

$$\left\{\bar{\varepsilon}_0^{(\mathrm{pl})}\right\}_e = \frac{1}{n_e}\sum_{\mathbf{r}\in\Omega_e}\bar{\varepsilon}_0^{(\mathrm{pl})}(\mathbf{r}) \tag{2}$$

where $\mathbf{r}$ is the position vector, and n_e is the number of points belonging to the e-th element domain Ω_e.

2.3. Macro-scale

The macro-scale model consists of a structural FE simulation, which computes the residual stress field and the associated distortions throughout the entire building process. The meshed part volume is sliced with planes perpendicular to the build direction, and all its elements are deactivated, i.e., their stiffness is reduced to a negligible fraction of its original value. Then, referring to Fig. 2, the slices are activated sequentially with the incompatible strain and initial equivalent plastic strain previously evaluated through the PSS method (Section 2.2). The model slices are unrelated to the actual process layers, and their number is selected based on a convergence criterion constrained by the computational resources available.

Algorithm 1 Pointwise strain superposition procedure

Input: x, y, z, A, B, F, T_{relax}

$\varepsilon_{ij}^{(\text{in})} \leftarrow 0$ ▷ Initialization
$\bar{\varepsilon}_0^{(\text{pl})} \leftarrow 0$
$r \leftarrow \begin{bmatrix} x & y & z \end{bmatrix}^\intercal$
for $l \leftarrow 1$ **to** n_l **do**
  $a \leftarrow \begin{bmatrix} A_{l1} & A_{l2} & A_{l3} \end{bmatrix}^\intercal$ ▷ Scan line properties
  $b \leftarrow \begin{bmatrix} B_{l1} & B_{l2} & B_{l3} \end{bmatrix}^\intercal$
  $n \leftarrow \dfrac{b-a}{\|b-a\|}$
  $f \leftarrow F_l$
  if $0 \leq n^\intercal(r-a) \leq \|b-a\| \wedge z \leq A_{l3}$ **then**
    $p \leftarrow r - a - (n^\intercal(r-a))\,n$ ▷ Projection
    $\varepsilon_{ij}^{(\text{el})} \leftarrow \varepsilon_{ij,f}^{(\text{el})}(p)$ ▷ Interpolation
    $\varepsilon_{ij}^{(\text{pl})} \leftarrow \varepsilon_{ij,f}^{(\text{pl})}(p)$
    $T_{\max} \leftarrow T_{\max,f}(p)$
    if $T_{\max} > T_{\text{relax}}$ **then** ▷ Relaxation
      $\varepsilon_{ij}^{(\text{in})} \leftarrow 0$
      $\bar{\varepsilon}_0^{(\text{pl})} \leftarrow 0$
    end if
    if $\operatorname{tr}\left(\varepsilon_{ij}^{(\text{el})}\right) > \operatorname{tr}\left(-\varepsilon_{ij}^{(\text{in})}\right)$ **then** ▷ Incompatible strain
      $\varepsilon_{ij}^{(\text{in})} \leftarrow -R^\intercal \varepsilon_{ij}^{(\text{el})} R$
    end if
    $\bar{\varepsilon}_0^{(\text{pl})} \leftarrow \max\left(\bar{\varepsilon}_0^{(\text{pl})}, \sqrt{\frac{2}{3}}\left\|\varepsilon_{ij}^{(\text{pl})}\right\|\right)$ ▷ Initial equivalent plastic strain
  end if
end for
return $\varepsilon_{ij}^{(\text{in})}$, $\bar{\varepsilon}_0^{(\text{pl})}$

Regarding the boundary conditions, a fixed support (replaced by weak springs during post-processing) on the base plate boundaries is used rather than simplified bolt connections whenever the base plate is much stiffer than the printed part. Every node that does not belong to the active elements is fully constrained to maintain the top surface of each slice at its nominal shape and size until activation. Lastly, the part removal is simulated by progressively detaching the bonded contact elements located at the interface with the base plate.

3. Validation

We tested our simulation strategy with various materials, geometries, and process parameters. Here we only report the results obtained for the three specimens represented in Fig. 3 made of selective laser melted Inconel 718 with the process parameters listed in Table 1. For reference, Fig. 4 shows the longitudinal and transverse residual stress components resulting from the meso-scale simulation of a single scan line in the x-direction (Section 2.1) performed with the above process parameters and the material properties provided in [3, 4, 5] under the hypothesis of multilinear isotropic hardening. This particular simulation was used to define the interpolation functions of the PSS method for all the applications presented hereinafter.

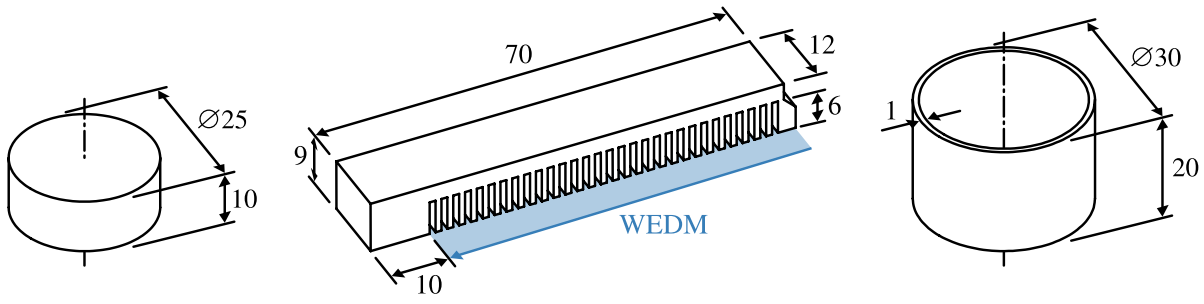

(a) Cylinder **(b)** Cantilever **(c)** Hollow cylinder

Figure 3. Validation specimens – the blue arrow in **b** indicates the wire cut performed on the cantilever supports after the building process (the other two specimens remain fully attached to the base plate).

Table 1. Main process parameters [6].

Parameter	Value
Nominal layer thickness	40 µm
Generalized beam diameter [7]	100 µm
Hatch distance (i.e., distance between adjacent scan lines)	110 µm
Hatch angle (i.e., angle between the scanning directions of two consecutive layers)	0°, 67°
Inskin power	285 W
Inskin speed	0.96 m s^{-1}
Preheating temperature	353 K

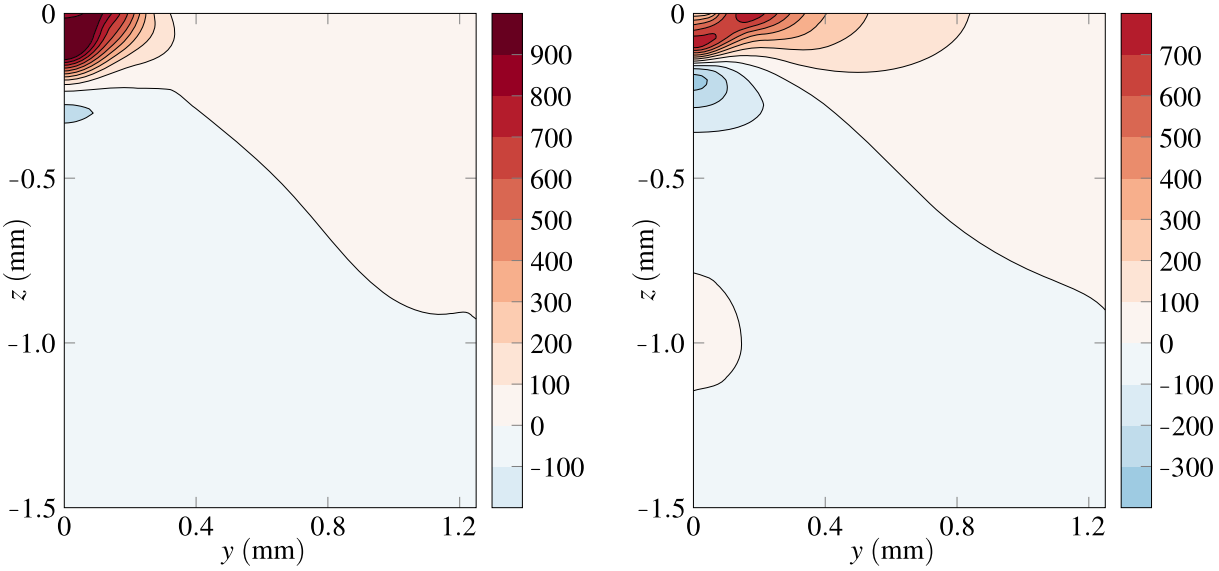

(a) Longitudinal stress component σ_{xx} (MPa) **(b)** Transverse stress component σ_{yy} (MPa)

Figure 4. Longitudinal and transverse residual stress components resulting from the meso-scale simulation of a single scan line in the x-direction performed on Inconel 718 with the process parameters listed in Table 1. Both results are represented only for $y \geq 0$ since they are symmetric about $y = 0$.

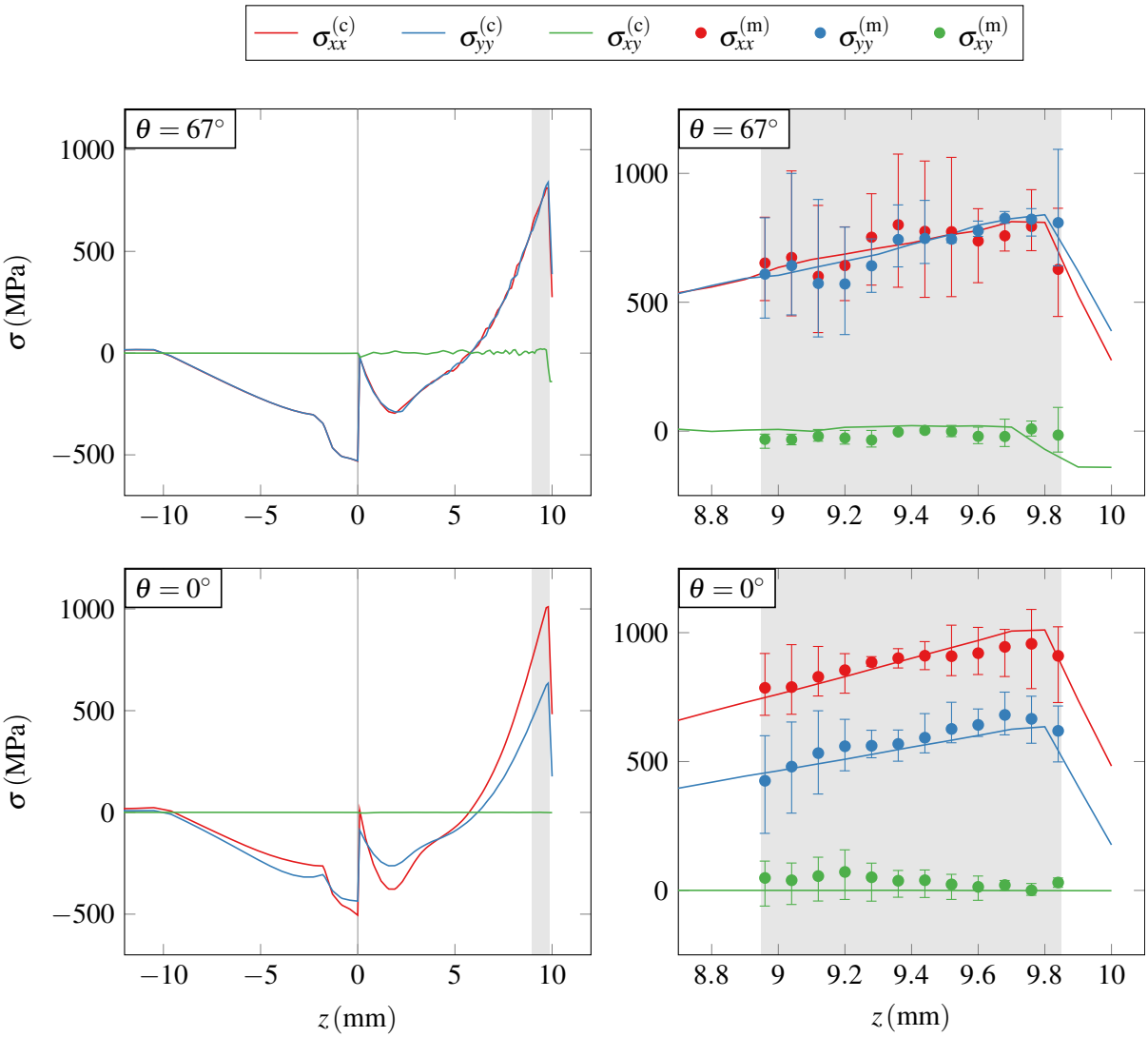

Figure 5. Computed $\sigma_{ij}^{(c)}$ and measured $\sigma_{ij}^{(m)}$ stress components near the axis of the cylindrical specimen. The z-axis is aligned with the build direction and originates at the interface between the specimen and the base plate. The results shown at the top of the figure were obtained with a hatch angle $\theta = 67°$, while the others refer to a uniform scanning strategy ($\theta = 0°$) oriented in the x-direction.

3.1. Surface stress

Figure 5 compares the computed and measured stress components near the axis of the cylindrical specimen of Fig. 3a printed with a hatch angle θ of 67° and 0°. The reference frame originates at the interface between the specimen and the base plate, its z-axis is aligned with the build direction, and its x-axis is oriented in the scanning direction for $\theta = 0°$. On these premises, the xx, yy, and xy stress components were measured within a depth range of approximately 0.15–1.05 mm below the top surface of eight samples (four for each scanning strategy) with the Blind Hole Drilling (BHD) method [8].

The rotated scanning strategy produces an approximately equibiaxial residual stress field, while the in-plane principal stresses differ even by 300 MPa for $\theta = 0°$ with the major principal stress oriented in the scanning direction. In both cases, the normal stresses peak around a depth of 0.2 mm, and, according to the simulations, they decrease sharply when approaching the top surface of the cylindrical specimen.

Unfortunately, the loss of accuracy of the BHD method at low hole depth-to-diameter ratios, together with the surface preparation needed to establish the zero-depth across the high surface roughness, meant that we were unable to verify this last result. Nevertheless, whenever reliable, the measured and computed stresses are perfectly consistent with one another for both scanning strategies.

From a qualitative perspective, the in-plane normal stresses decrease initially with depth since each new layer compresses its substrate. Then, past a certain threshold, there is enough compressed material to balance the overlying tensioned region, and the underlying stress field is progressively relieved. This turnaround is clearly visible at $z \approx 2\,\text{mm}$ in Fig. 5 along with the stress discontinuity occurring at the interface between the specimen and the base plate ($z = 0$). Although such depths were completely out of reach for the employed BHD setup[2], we verified that our simulation strategy could at least reproduce the structural effects of the considered scanning processes down to about 1 mm below the top layer. However, if the building process remains self-similar regardless of the printing height, there is no clear reason to doubt the validity of the structural solution across the entire depth range.

3.2. Cantilever deflection

Assessing the simulation accuracy on the stress gradient in the build direction based solely on the reported BHD measures is nevertheless rather difficult, if not impossible, given their limited precision and depth range. Such an assessment would confirm whether the simulation strategy is able to reproduce the global stress field evolution throughout the entire building process and to what extent. For this purpose, a very convenient measure indirectly related to the above stress gradient is the end deflection of a horizontally oriented cantilever-shaped specimen (e.g., Fig. 3b) after its removal. In fact, the fraction of elastic energy associated with bending and axial stresses is progressively released when detaching the supports from the base plate. This causes the cantilever to bend and contract towards a self-balanced configuration. Unlike for stresses, measuring millimetric end deflections is extremely straightforward, and even the most rudimentary equipment typically guarantees lower relative errors than the BHD method. However, this measure is integral (rather than localized), does not provide the actual stress distribution, and requires a specimen specifically designed to achieve a measurable end deflection together with a uniform stress gradient in the build direction across the entire top flange (boundary regions excluded).

Figure 6 compares the computed $\delta_z^{(\mathrm{c})}$ and measured $\delta_z^{(\mathrm{m})}$ end deflections for the two scanning strategies defined in Section 3.1. In the case of $\theta = 0^\circ$, the scan lines are aligned with the longest edges of the top flange to maximize its bending as dictated by the BHD results. Given a constant FE mesh, the computed end deflections converge when the number of slices is increased. At 60 slices $\delta_z^{(\mathrm{c})}(67^\circ) = 3.11\,\text{mm}$ and $\delta_z^{(\mathrm{c})}(0^\circ) = 3.91\,\text{mm}$, whereas the respective experimental ranges (measured via CMM[3] on three samples for each scanning strategy) are $3.00 \pm 0.04\,\text{mm}$ and $3.67 \pm 0.05\,\text{mm}$. As a result, the relative error is about 2% in the first case and 5% in the second, which is impressive considering the significant uncertainties regarding the input parameters and material properties. We can therefore conclude that the presented simulation method is capable of reproducing the stress gradient in the build direction across at least the 3 mm thickness of the top flange.

3.3. Hollow cylinder distortion

As a final test, we assessed the model accuracy on part distortions, i.e., the differences between the as-built and nominal geometries. In fact, predicting out-of-tolerance conditions already at the design stage is a key benefit of process simulation tools, especially for high-mix low-volume additive technologies. Hollow cylinders, such as the one represented in Fig. 3c, are particularly suitable for this purpose whenever the scanning path has no preferred directions (e.g., for $\theta = 67^\circ$). In this case, the as-built geometry remains roughly axisymmetric and can be fully described by expressing its inner and outer radii

[2] Rectangular strain gauge rosette HBM RY61K (0°/45°/90°) with a nominal hole diameter of 1.8 mm.
[3] Coordinate Measuring Machine.

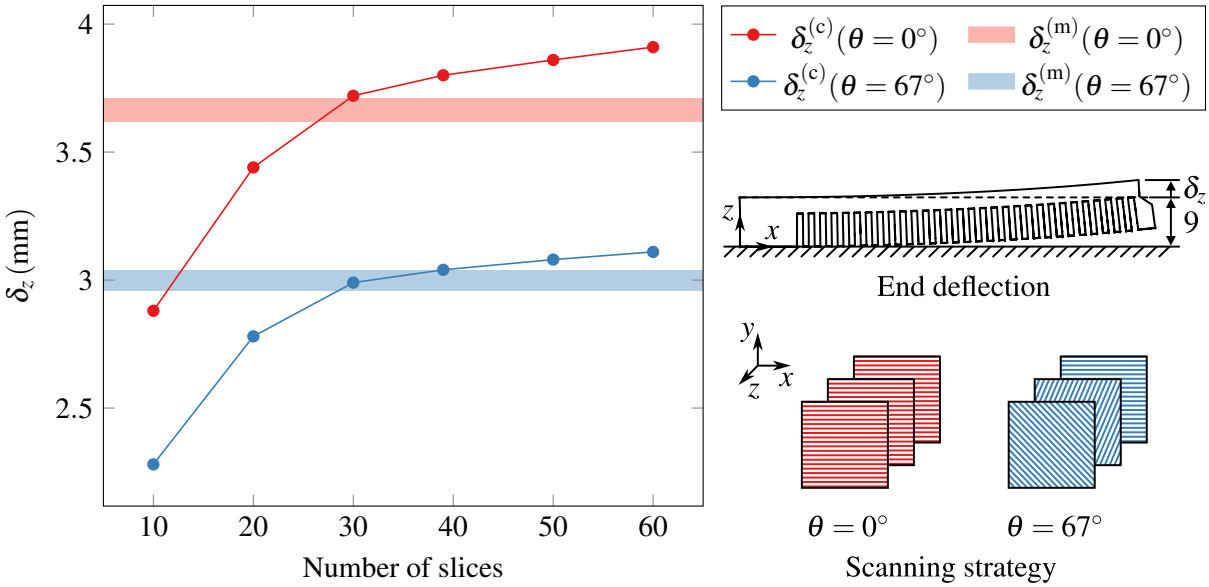

Figure 6. Measured $\delta_z^{(m)}$ and computed $\delta_z^{(c)}$ end deflection varying the number of slices with a fixed mesh for two scanning strategies of hatch angle $\theta = 0°$ and $67°$.

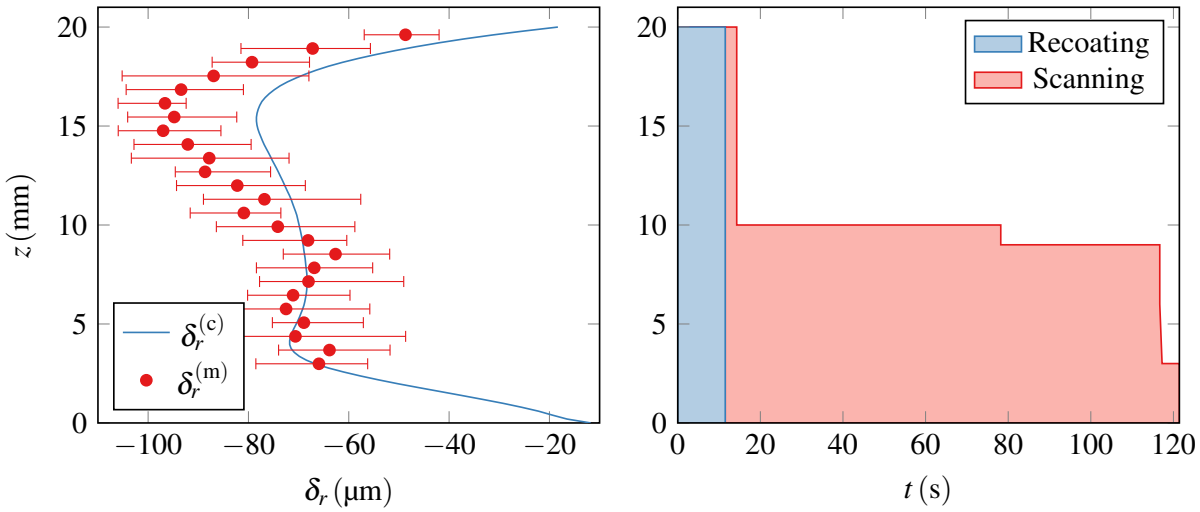

Figure 7. Computed $\delta_r^{(c)}$ and measured $\delta_r^{(m)}$ distortions of the hollow cylinder, beside the approximate build time per layer, as functions of the height above the base plate z. The distortion δ_r is defined as the difference between the as-built and nominal outer radii.

as functions of the height above the base plate z. Furthermore, the small thickness reduces the bending effects (shown in the cantilever-shaped specimen) with respect to the in-plane layer contractions.

Figure 7 compares the computed $\delta_r^{(c)}$ and measured $\delta_r^{(m)}$ distortions of the hollow cylinder represented in Fig. 3c, where δ_r is the difference between the as-built and nominal outer radii. More specifically, we measured a total of nine profiles over three samples printed with a hatch angle $\theta = 67°$. The swept envelope of the CMM feeler impeded radial measures for $z \leq 2.5\,\text{mm}$. Below this limit, $\delta_r^{(c)}$ rapidly decreases in modulus approaching $z = 0$ due to the base plate constraining effect. A similar behavior, but with a different cause, is observable for $z \to 20\,\text{mm}$ since each layer is printed at nominal

size and then shrinks while compressing its substrate. This initially increases the in-plane contraction as more and more layers get deposited above the considered height. However, as observed for stresses in Section 3.1, such distortion trend is gradually reversed past the compressive stress front.

Although the simulation predicts the final shape of the outer profile, it underestimates the radial contraction for $z \geq 10\,\text{mm}$. The reason for this loss of accuracy is likely related to the macro-scale thermal history, which is completely neglected by our simulation strategy. In support of this, Fig. 7 shows the approximate build time per layer across the entire printing height. Since all the specimens of Fig. 3 were printed in the same job, and the hollow cylinders were the only ones exceeding 10 mm in height, the scanning time dropped to 2.78 s at the 251st layer ($z = 10.04\,\text{mm}$). Adding a recoating time of about 11.5 s, we obtain an average cooling time of 14.28 s, which might not have been enough for the substrate to reach the preheating temperature. The resulting thermal difference may have violated the position independence hypothesis and therefore undermined the accuracy of the model for $z \geq 10\,\text{mm}$.

4. Conclusions

We have described a multi-scale method for simulating PBF processes. The method was able to predict the process-induced stresses and distortions on selective laser melted Inconel 718. The surface stresses computed on a cylindrical specimen were in agreement with the BHD measures for two different scanning strategies with hatch angles of 0° and 67°. The simulation also predicted the end deflection of a cantilever-shaped specimen after removing its supports with an error of about 4% and 2% for the above scanning strategies. Lastly, the method provided a first-order approximation of the distortion profile for a hollow cylinder printed with a hatch angle of 67°. In the latter case, however, there was a significant decrease in accuracy from a height of about 10 mm above the base plate upwards. We believe that the underestimation of the in-plane contraction in this region may be due to an insufficient cooling time as a result of the reduced scanning area. If true, the above issue should be limited solely to cases where the sum of the recoating and scanning times does not exceed a safety threshold (typically in the order of a few tens of seconds, depending on the required accuracy). Under such circumstances, there is no choice but to reject the position independence hypothesis and combine the PSS method with a macro-scale thermal analysis based on the actual build times.

In conclusion, if implemented within a standalone or integrated process simulation software, the validated method could help reduce the number of failed iterations often needed before achieving a successful print. In a few cases, however, a macro-scale thermal analysis might be useful to compensate for some of its weaknesses and increase accuracy at the expense of computational efficiency.

Acknowledgments

This research was funded by the TPS Innovation Department of Baker Hughes as part of its long and fruitful collaboration with the University of Pisa. The authors express their gratitude to everyone involved in the project at Baker Hughes and the University of Pisa.

References

[1] Goldak J A, Chakravarti A and Bibby M 1984 *Metall. Mater. Trans.* B **15** 299–305
[2] Goldak J A and Akhlaghi M 2005 *Computational Welding Mechanics* (New York: Springer)
[3] Hosaeus H, Seifter A, Kaschnitz E and Pottlacher G 2001 *High Temp. – High Press.* **33** 405–10
[4] Valencia J J and Quested P N 2008 *ASM Handbook: Casting* **15** 468–81
[5] Dunbar A J, Denlinger E R, Gouge M F and Michaleris P 2016 *Addit. Manuf.* **12**(A) 108–20
[6] Chen Q, Liang X, Hayduke D, Liu J, Cheng L, Oskin J, Whitmore R and To A C 2019 *Addit. Manuf.* **28** 406–18
[7] International Standards 2005 *ISO 11146-2:2005(E) Lasers and laser-related equipment – Test methods for laser beam widths, divergence angles and beam propagation ratios – General astigmatic beams* (Geneva: International Organization for Standardization)
[8] International Standards 2013 *ASTM E837-13a Standard Test Method for Determining Residual Stresses by the Hole-Drilling Strain-Gage Method* (West Conshohocken: ASTM International)